

A high-order upwind control-volume method based on integrated RBFs for fluid-flow problems

N. Mai-Duy* and T. Tran-Cong

Computational Engineering and Science Research Centre

Faculty of Engineering and Surveying

University of Southern Queensland, Toowoomba, QLD 4350, Australia

Short title: Integrated-RBF based Upwind Control Volume Method

Submitted to *International Journal for Numerical Methods in Fluids*,

15-Jun-2010; revised, 28-Sep-2010

*Corresponding author: E-mail nam.mai-duy@usq.edu.au, Telephone +61 7 4631 2748, Fax +61 7 4631 2526

Summary This paper is concerned with the development of a high-order upwind conservative discretisation method for the simulation of flows of a Newtonian fluid in two dimensions. The fluid-flow domain is discretised using a Cartesian grid from which non-overlapping rectangular control-volumes are formed. Line integrals arising from the integration of the diffusion and convection terms over control volumes are evaluated using the middle-point rule. One-dimensional integrated radial basis function schemes using the multiquadric basis function are employed to represent the variations of the field variables along the grid lines. The convection term is effectively treated using an upwind scheme with the deferred-correction strategy. Several highly-nonlinear test problems governed by the Burgers and the Navier-Stokes equations are simulated, which show that the proposed technique is stable, accurate and converges well.

Key words: integrated RBF, Cartesian grid, control volume, upwind scheme, deferred correction technique, high-order approximation

1 Introduction

The control-volume (CV) formulation has been extensively used in the discretisation of partial differential equations (PDEs) governing heat-transfer and fluid-flow problems (e.g. [1,2]). As discussed in [1], there are four basic rules that the discretisation equations should obey to ensure a physically realistic solution: (i) Consistency at CV faces, (ii) Positive coefficients (physically meaningful solutions), (iii) Negative-slope linearisation of the source term and (iv) Sum of the neighbour coefficients. It is noted that these rules are sufficient conditions only. For convection-dominant flows, special attention should be given to the treatment of the convection term. If a linear profile (i.e. central differencing) is used, the second rule will be violated. In this case, some of the coefficients may be negative and the associated coefficient matrix may not be diagonally dominant. As a result, convergent difficulties are added if one uses iterative methods to solve the linearised

algebraic system. Recognising these, various schemes that take the influence of the upwind information of the flow into account, e.g. the upwind differencing [3], power-law [4] and QUICK [5] schemes, have been developed.

The original upwind (upwind-difference/upstream-difference/donor-cell) scheme, which simply replaces the face value of the convected property with its value at the grid point on the upwind side of the face, is able to ensure positive coefficients. However, this scheme is only first-order accurate and causes a false diffusion/artificial viscosity. The power-law scheme, which can also guarantee the positivity of all coefficients, has a blended first/second order accuracy. When the local grid Peclet numbers exceed a value of 6, this scheme switches to the first-order upwinding scheme and the physical diffusion is therefore suppressed [6]. Such formulations do not work well for the cases where the flow streamlines are not closely aligned with the grid lines. On the other hand, the QUICK scheme employs a quadratic interpolation at three consecutive nodes (the two nodes located on either side of the face and the adjacent node on the upstream side) to represent the convective term. The QUICK scheme results in a better accuracy and avoids the stability problems of central differencing. Unlike upwind differencing, this quadratic interpolation scheme may produce negative coefficients and as a result its coefficient matrix may not be diagonally dominant.

It is highly desirable to have upwind numerical schemes that possess the convergence properties of first-order schemes (the solution evolves in a stable manner, i.e. always physically meaningful) and the accuracy properties of high-order schemes (accurate solutions are obtained using relatively coarse meshes). A simple, but effective way to achieve these objectives is to use the deferred correction strategy (e.g. [7,8]). A high-order approximate expression for computing the convected face value is cast as the upstream value (the first-order upwinding scheme) and the streamwise correction term which are then treated implicitly and explicitly, respectively. This strategy can be applied to any kind of high-order upwind schemes.

Radial basis functions (RBFs) have been extensively used in solving differential problems (e.g. [9]). These approximators are able to work well (i.e. providing fast convergence) with gridded and scattered data points especially for regular node arrangements. The RBF approximations can be constructed through differentiation (e.g. [10]) or integration (e.g. [11,12,13]). The latter has the ability to avoid the reduction in convergence rate caused by differentiation and to provide an effective way of implementing derivative boundary values. Integrated RBFs (IRBFs) were successfully introduced into the CV formulation [14]. All of our previous IRBF works treated the diffusion and convection terms implicitly and explicitly, respectively. In this study, the diffusion term is approximated using global and local one-dimensional IRBF schemes, namely Scheme 1 and Scheme 2, respectively. The convection term is effectively treated here by a high-order upwind scheme incorporating global 1D-IRBFs with the deferred-correction strategy. The proposed schemes achieve both good accuracy and stability properties.

The remainder of the paper is organised as follows. Brief reviews of the CV formulation and 1D-IRBFs are given in Sections 2 and 3, respectively. Section 4 describes the two proposed discretisation schemes. In Section 5, two examples - heat transfer and fluid flow - are presented to demonstrate the attractiveness of the present implementation. Section 6 concludes the paper.

2 Control-volume formulation

Consider the following convection-diffusion equation

$$\frac{\partial}{\partial t}(\rho\phi) + \nabla \cdot (\rho\hat{v}\phi) - \nabla \cdot (\kappa\nabla\phi) + R = 0, \quad \hat{x} \in \Omega, \quad (1)$$

where ϕ is the field variable; t the time; ρ the density; \hat{v} the convection velocity vector; κ the diffusion coefficient; R the source term; \hat{x} the position vector and Ω the domain of

interest.

The above equation presents the conservation principle for ϕ over an infinitesimal control volume (i.e. there is a balance between the rate of change of ϕ , the convective flux rate, the diffusion flux rate and the generation rate). By directly integrating (1) over a control volume of the grid point P , Ω_P , the following equation is obtained

$$\int_{\Omega_P} \left(\frac{\partial}{\partial t}(\rho\phi) + \nabla \cdot (\rho\hat{v}\phi) - \nabla \cdot (\kappa\nabla\phi) + R \right) d\Omega_P = 0, \quad (2)$$

which possesses the conservative property for ϕ for a finite control volume.

Applying the Gauss divergence theorem to (2) results in

$$\frac{\partial}{\partial t} \int_{\Omega_P} (\rho\phi) d\Omega_P + \int_{\Gamma_P} (\rho\hat{v}\phi) \cdot \hat{n} d\Gamma_P - \int_{\Gamma_P} (\kappa\nabla\phi) \cdot \hat{n} d\Gamma_P + \int_{\Omega_P} R d\Omega_P = 0, \quad (3)$$

where Γ_P is the boundary of Ω_P ; \hat{n} the unit outward vector normal to Γ_P and $d\Gamma_P$ a differential element of Γ_P . The governing differential equation (1) is thus transformed into a CV form (2)/(3). It is noted that no approximation is made at this stage.

3 One-dimensional IRBF scheme

The basic idea of the integral RBF scheme is to decompose the highest-order derivatives of ϕ in a given differential equation (e.g. second-order derivatives for the convection-diffusion equation (1)) into RBFs. Consider a univariate function $\phi(x)$. The present 1D-IRBF scheme starts with

$$\frac{d^2\phi(x)}{dx^2} = \sum_{i=1}^N w_i I_i^{(2)}(x), \quad (4)$$

where N is the number of RBFs, $\{w_i\}_{i=1}^N$ the set of network weights, and $\{I_i^{(2)}(x)\}_{i=1}^N$ the set of RBFs. Expressions for the first-order derivative and function itself are then obtained through integration

$$\frac{d\phi(x)}{dx} = \sum_{i=1}^N w_i I_i^{(1)}(x) + c_1, \quad (5)$$

$$\phi(x) = \sum_{i=1}^N w_i I_i^{(0)}(x) + c_1 x + c_2, \quad (6)$$

where $I_i^{(1)}(x) = \int I_i^{(2)}(x) dx$, $I_i^{(0)}(x) = \int I_i^{(1)}(x) dx$; and (c_1, c_2) are the constants of integration. It is noted that the superscript $(.)$ is used to indicate the derivative order of ϕ . In the present work, 1D-IRBFs are implemented with the multiquadric (MQ) function and one has

$$I_i^{(2)}(x) = \sqrt{(x - c_i)^2 + a_i^2}, \quad (7)$$

$$I_i^{(1)}(x) = \frac{(x - c_i)}{2} A + \frac{a_i^2}{2} B, \quad (8)$$

$$I_i^{(0)}(x) = \left(\frac{-a_i^2}{3} + \frac{(x - c_i)^2}{6} \right) A + \frac{a_i^2(x - c_i)}{2} B, \quad (9)$$

where c_i and a_i are the centre and the width of the i th MQ, respectively; $A = \sqrt{(x - c_i)^2 + a_i^2}$; and $B = \ln \left((x - c_i) + \sqrt{(x - c_i)^2 + a_i^2} \right)$.

Evaluation of (4)-(6) at a set of collocation points $\{x_i\}_{i=1}^N$ (also a set of the MQ centres here, $\{x_i\}_{i=1}^N \equiv \{c_i\}_{i=1}^N$) leads to

$$\widehat{\frac{d^2\phi}{dx^2}} = \widehat{\mathcal{I}}^{(2)} \widehat{\alpha}, \quad (10)$$

$$\widehat{\frac{d\phi}{dx}} = \widehat{\mathcal{I}}^{(1)} \widehat{\alpha}, \quad (11)$$

$$\widehat{\phi} = \widehat{\mathcal{I}}^{(0)} \widehat{\alpha}, \quad (12)$$

where

$$\begin{aligned}\widehat{\mathcal{I}}^{(2)} &= \begin{bmatrix} I_1^{(2)}(x_1), & I_2^{(2)}(x_1), & \cdots, & I_N^{(2)}(x_1), & 0, & 0 \\ I_1^{(2)}(x_2), & I_2^{(2)}(x_2), & \cdots, & I_N^{(2)}(x_2), & 0, & 0 \\ \vdots & \vdots & \ddots & \vdots & \vdots & \vdots \\ I_1^{(2)}(x_N), & I_2^{(2)}(x_N), & \cdots, & I_N^{(2)}(x_N), & 0, & 0 \end{bmatrix}, \\ \widehat{\mathcal{I}}^{(1)} &= \begin{bmatrix} I_1^{(1)}(x_1), & I_2^{(1)}(x_1), & \cdots, & I_N^{(1)}(x_1), & 1, & 0 \\ I_1^{(1)}(x_2), & I_2^{(1)}(x_2), & \cdots, & I_N^{(1)}(x_2), & 1, & 0 \\ \vdots & \vdots & \ddots & \vdots & \vdots & \vdots \\ I_1^{(1)}(x_N), & I_2^{(1)}(x_N), & \cdots, & I_N^{(1)}(x_N), & 1, & 0 \end{bmatrix}, \\ \widehat{\mathcal{I}}^{(0)} &= \begin{bmatrix} I_1^{(0)}(x_1), & I_2^{(0)}(x_1), & \cdots, & I_N^{(0)}(x_1), & x_1, & 1 \\ I_1^{(0)}(x_2), & I_2^{(0)}(x_2), & \cdots, & I_N^{(0)}(x_2), & x_2, & 1 \\ \vdots & \vdots & \ddots & \vdots & \vdots & \vdots \\ I_1^{(0)}(x_N), & I_2^{(0)}(x_N), & \cdots, & I_N^{(0)}(x_N), & x_N, & 1 \end{bmatrix}; \\ \widehat{\alpha} &= (w_1, w_2, \cdots, w_N, c_1, c_2)^T;\end{aligned}$$

and

$$\begin{aligned}\widehat{\frac{d^k \phi}{dx^k}} &= \left(\frac{d^k \phi_1}{dx^k}, \frac{d^k \phi_2}{dx^k}, \cdots, \frac{d^k \phi_N}{dx^k} \right)^T, \quad k = (1, 2), \\ \widehat{\phi} &= (\phi_1, \phi_2, \cdots, \phi_N)^T,\end{aligned}$$

in which $d^k \phi_i / dx^k = d^k \phi(x_i) / dx^k$ and $\phi_i = \phi(x_i)$ with $i = (1, 2, \cdots, N)$.

Since the constants of integration are unknown, we treat them like the RBF weights. The present coefficient vector $\widehat{\alpha}$ is thus larger than that of the conventional/differential approach. As a result, extra equations can be added to the system that represents the

conversion of the RBF weight space into the physical space

$$\begin{pmatrix} \hat{\phi} \\ \hat{e} \end{pmatrix} = \begin{bmatrix} \hat{\mathcal{I}}^{(0)} \\ \hat{\mathcal{K}} \end{bmatrix} \hat{\alpha} = \hat{\mathcal{C}} \hat{\alpha}, \quad (13)$$

where $\hat{e} = (e_1, e_2)^T$ is a vector representing extra information (e.g. normal derivatives and differential equations at the boundaries); $\hat{e} = \hat{\mathcal{K}} \hat{\alpha}$; $\hat{\phi}$, $\hat{\mathcal{I}}^{(0)}$ and $\hat{\alpha}$ defined as before; and $\hat{\mathcal{C}}$ the conversion matrix. It can be seen from (13) that the approximate solution ϕ is collocated at the whole set of centres. Solving (13) for $\hat{\alpha}$ yields

$$\hat{\alpha} = \hat{\mathcal{C}}^{-1} \begin{pmatrix} \hat{\phi} \\ \hat{e} \end{pmatrix}, \quad (14)$$

where $\hat{\mathcal{C}}^{-1}$ is the inverse or pseudo-inverse of $\hat{\mathcal{C}}$, depending on its dimensions. The cost for computing the pseudo inverse is greater than that for the inverse. If there are some extra values (e.g. nodal boundary derivatives of the stream function used in the derivation of computational boundary conditions for the vorticity, which will be presented in detail later), the matrix $\hat{\mathcal{C}}$ will be square. If there is no extra information (\hat{e} a null vector), the matrix $\hat{\mathcal{C}}$ will be underdetermined and its pseudo inverse can be computed by the SVD technique. Fortunately, the present approximations are based on 1D-IRBFs rather than global 2D-IRBFs so that the conversion matrices here have much smaller sizes than the final system matrix.

Substitution of (14) into (4)-(6) leads to

$$\phi(x) = \left(I_1^{(0)}(x), I_2^{(0)}(x), \dots \right) \hat{\mathcal{C}}^{-1} \begin{pmatrix} \hat{\phi} \\ \hat{e} \end{pmatrix}, \quad (15)$$

$$\frac{\partial \phi(x)}{\partial x} = \left(I_1^{(1)}(x), I_2^{(1)}(x), \dots \right) \hat{\mathcal{C}}^{-1} \begin{pmatrix} \hat{\phi} \\ \hat{e} \end{pmatrix}, \quad (16)$$

$$\frac{\partial^2 \phi(x)}{\partial x^2} = \left(I_1^{(p)}(x), I_2^{(p)}(x), \dots \right) \hat{\mathcal{C}}^{-1} \begin{pmatrix} \hat{\phi} \\ \hat{e} \end{pmatrix}. \quad (17)$$

They can be rewritten in the form

$$\phi(x) = \sum_{i=1}^N \varphi_i(x) \phi_i + \varphi_{N+1}(x) e_1 + \varphi_{N+2}(x) e_2, \quad (18)$$

$$\frac{\partial \phi(x)}{\partial x} = \sum_{i=1}^N \frac{d\varphi_i(x)}{dx} \phi_i + \frac{d\varphi_{N+1}(x)}{dx} e_1 + \frac{d\varphi_{N+2}(x)}{dx} e_2, \quad (19)$$

$$\frac{\partial^2 \phi(x)}{\partial x^2} = \sum_{i=1}^N \frac{d^2 \varphi_i(x)}{dx^2} \phi_i + \frac{d^2 \varphi_{N+1}(x)}{dx^2} e_1 + \frac{d^2 \varphi_{N+2}(x)}{dx^2} e_2, \quad (20)$$

where $\{\varphi_i(x)\}_{i=1}^{N+2}$ is the set of basis functions in the physical space.

4 Proposed method

The problem domain is discretised using a Cartesian grid. Non-overlapping control volumes of rectangular shapes are generated around grid nodes. We employ the middle-point rule to evaluate integrals of convection and diffusion terms. For integrals involving the rates of change and generation, the value of the quantity at a grid point is assumed to prevail over its control volume. The time derivative term is approximated by means of

the first-order backward Euler implicit formula. Equation (3) thus becomes

$$\begin{aligned} & \frac{\rho_P \Delta A_P}{\Delta t} (\phi_P - \phi_P^0) + [(\rho u \phi)_e \Delta y - (\rho u \phi)_w \Delta y + (\rho v \phi)_n \Delta x - (\rho v \phi)_s \Delta x] - \\ & \left[\left(\kappa \frac{\partial \phi}{\partial x} \right)_e \Delta y - \left(\kappa \frac{\partial \phi}{\partial x} \right)_w \Delta y + \left(\kappa \frac{\partial \phi}{\partial y} \right)_n \Delta x - \left(\kappa \frac{\partial \phi}{\partial y} \right)_s \Delta x \right] + R_P \Delta A_P = 0, \quad (21) \end{aligned}$$

where the superscript 0 represents the value obtained from the previous time level; the subscripts e, w, n and s denote the values of the property at the middle points of the east, west, north and south faces of a control volume; ΔA_P the area of Ω_P ; R_P the value of R at node P ; and u and v the x - and y -component of \hat{v} .

It can be seen that expressions for computing the interface values on the x - and y -grid lines have similar forms. Thus, in the following, details will be given for an x -grid line only.

4.1 Diffusion approximations

The diffusion term is treated implicitly. In regions where the convection strength is relatively large, the role of the diffusion term is less important. For most cases of practical interest, the actual component grid Peclet numbers are large almost everywhere in the flow field [6]. We therefore employ not only global 1D-IRBFs (Scheme 1) but also local 1D-IRBFs with three points (Scheme 2) for the approximation of the third term on the LHS of (21) (i.e. the approximating form of the diffusion term).

4.1.1 Scheme 1

Using (19), the face value is computed as

$$\left(\frac{\partial\phi}{\partial x}\right)_e = \sum_{i=1}^{N_x} \frac{d\varphi_i(x_e)}{dx} \phi_i + \frac{d\varphi_{N_x+1}(x_e)}{dx} e_1 + \frac{d\varphi_{N_x+2}(x_e)}{dx} e_2, \quad (22)$$

$$\left(\frac{\partial\phi}{\partial x}\right)_w = \sum_{i=1}^{N_x} \frac{d\varphi_i(x_w)}{dx} \phi_i + \frac{d\varphi_{N_x+1}(x_w)}{dx} e_1 + \frac{d\varphi_{N_x+2}(x_w)}{dx} e_2, \quad (23)$$

where N_x is the total number of nodes on the x -grid line. These approximations are global and hence guarantee that the flux is continuous across the interface between any two adjoining control volumes (the first CV rule).

4.1.2 Scheme 2

The face value is evaluated as

$$\left(\frac{\partial\phi}{\partial x}\right)_e = \sum_{i=1}^3 \frac{d\varphi_i(x_e)}{dx} \phi_i + \frac{d\varphi_4(x_e)}{dx} e_1 + \frac{d\varphi_5(x_e)}{dx} e_2, \quad (24)$$

$$\left(\frac{\partial\phi}{\partial x}\right)_w = \sum_{i=1}^3 \frac{d\varphi_i(x_w)}{dx} \phi_i + \frac{d\varphi_4(x_w)}{dx} e_1 + \frac{d\varphi_5(x_w)}{dx} e_2. \quad (25)$$

These approximations are local and constructed on overlapping regions that are defined between the west and east grid points of node P . The resultant matrix of Scheme 2 is much more sparse than that of Scheme 1.

4.2 Convection approximations

For both Scheme 1 and Scheme 2, the convection term will be handled in the same manner. In the case that the strength of convection is much greater than the strength of diffusion, the second term on the LHS of (21) (i.e. convection) is dominant and strongly affects the

stability of a numerical scheme. From the physical point of view, convection represents the flow from upstream to downstream. One can thus expect that the upstream nodal value of ϕ , denoted by ϕ_U , would make quite an impact on the value of ϕ at the interface, denoted by ϕ_f . It is noted that the subscript f can be e or w . We treat the convection term here by an upwind scheme incorporating global 1D-IRBFs with the deferred-correction strategy

$$\phi_f = \phi_U + \Delta\phi_f, \quad (26)$$

where

$$\Delta\phi_f = \sum_{i=1}^{U-1} \varphi_i(x_f) \phi_i^0 + (\varphi_U(x_f) - 1) \phi_U^0 + \sum_{i=U+1}^{N_x} \varphi_i(x_f) \phi_i^0 + \varphi_{N_x+1}(x_f) e_1 + \varphi_{N_x+2}(x_f) e_2,$$

in which $\{\phi_i^0\}_{i=1}^{N_x}$ are the nodal values of ϕ obtained from the previous time level. The streamwise correction term $\Delta\phi_f$ is therefore known at the current time level. Expression (26) ensures diagonal dominance for the resultant system of algebraic equations and approximate solutions can therefore evolve in a stable manner (i.e. solution is physically meaningful at all times). At convergence, the accuracy of ϕ_f is determined by the global 1D-IRBF scheme.

It can be seen that Scheme 2 has the same structure of the system matrix (i.e. the tridiagonal and pentadiagonal forms for 1D and 2D problems, respectively) as the standard CV techniques.

Scheme 1 and Scheme 2 are both constructed by means of 1D-IRBFs and point collocation so that all nodal values of the variable are forced to be satisfied in an exact manner. Numerical experiments show that the present discretisation equations obey the fourth CV rule, i.e. sum of the neighbour coefficients.

5 Numerical examples

The performance of the proposed discretisation schemes, i.e. Scheme 1 and Scheme 2, is studied through the solution of the Burgers and Navier-Stokes equations. The latter is taken in the stream-function and vorticity formulation. The grid size, h , is chosen as the MQ width. All PDEs under consideration here are subject to Dirichlet boundary conditions. The extra information vector \hat{e} in (13) is set to null for solving the PDEs and to derivative boundary values of the stream function for deriving computational boundary conditions for the vorticity. For comparison purposes, the standard CV techniques, where the diffusion term is discretised using central differences, are also employed here. If the convection term is treated using the original upwind version, we name it an UW-CD technique. If the convection term is treated using the central-difference formulation, it is then called an CD-CD technique. Scheme 2 can somehow serve as a tool to measure the relative performance of the upwind scheme based on 1D-IRBFs to those based on polynomials. Time-dependent equations are solved by the time-marching approach. A computed solution at a lower Reynolds number is used as the initial condition. For the special case of Stokes equations, the flow starts from rest. We utilise banded and iterative solvers to solve the algebraic equation sets.

5.1 Example 1

Consider the following non-linear Burgers equation

$$\frac{d\phi}{dt} + \phi \frac{d\phi}{dx} = \varepsilon \frac{d^2\phi}{dx^2}, \quad (27)$$

on the domain $x_A \leq x \leq x_B$ with Dirichlet boundary conditions, where ε is a given value. We consider steady flows, for which analytical solutions are given by

$$\phi(x) = -\tanh\left(\frac{x}{2\varepsilon}\right). \quad (28)$$

Calculations are carried out on uniformly-distributed nodes.

To investigate the convergence behaviour of the two present discretisation schemes, a global 1D-IRBF-based CV technique, where the diffusion and convection terms are respectively treated implicitly and explicitly, is also considered. This technique is referred to as the original IRBF version. As discussed earlier, the original IRBF version and Scheme 1 will give the same accuracy when the solutions are converged. For Scheme 2, the coefficient matrix is tridiagonal. When the discrete relative norm of ϕ between two successive time levels, tol , is less than 10^{-7} , the flow is considered to reach a steady state. Different time steps, namely 0.1, 0.05, 0.01, 0.005 and 0.001, are employed. Results are presented in Table 1, indicating that much larger time steps can be used with the present schemes. Scheme 1 works better than Scheme 2.

To assess accuracy of the two present schemes, we employ the UW-CD technique. The error is measured using the discrete relative norm of ϕ , denoted by $N_e(\phi)$, at a test set of 501 uniformly distributed points. Table 2 shows that the present schemes especially Scheme 1 significantly outperform the UW-CD technique regarding accuracy, i.e. up to two orders of magnitude for Scheme 1. In addition, Scheme 1 gives a very fast convergence, i.e. up to $O(h^{7.85})$, as shown in Table 3. A computed solution by Scheme 1 together with the exact solution at $\varepsilon = 10^{-3}$ are shown in Figure 1.

5.2 Example 2

Recirculating laminar incompressible flows of a Newtonian/non-Newtonian fluid in enclosed cavities have received a great deal of attention in fluid mechanics community as they can produce interesting flow features at different Reynolds/Weissenberg numbers. Examples of this type include lid-driven flows in square and triangular cavities. The top wall (lid) slides at a constant velocity. For such problems, at the two top corners, the velocity is discontinuous and the stress is unbounded, which poses great challenges for numerical simulation. This study is concerned with a Newtonian fluid and cavities of square and equilateral triangular shapes. The governing equations are employed in the form of the stream function (ψ) and vorticity (ω)

$$\omega = \nabla \cdot (\nabla \psi), \quad (29)$$

$$\frac{\partial \omega}{\partial t} + \nabla \cdot (\hat{v} \omega) = \frac{1}{R_e} \nabla \cdot (\nabla \omega), \quad (30)$$

where $\hat{v} = (u, v)^T = (\partial \psi / \partial y, -\partial \psi / \partial x)^T$ and R_e is the Reynolds number.

Boundary nodes are generated here using grid lines that pass through interior grid nodes. As a result, the set of RBF centres/collocation-points does not include the two top corners (the triangular cavity) and the four corners (the square cavity). By this simple treatment, it can be seen that infinite values of the vorticity do not enter the discrete system. 1D-IRBFs are employed on each grid line to represent the field variable and its derivatives in solving (29) and (30).

5.2.1 Square cavity

The stability of the flow in a square cavity has been extensively studied (e.g. [15]). Values of critical parameters at which the flow becomes unstable were obtained through hydrodynamic stability analyses. Critical Reynolds numbers were found in the range of

7704 to 8031. In this study, the time-dependent Navier-Stokes equations are solved for a wide range of R_e , namely (100, 1000, 3200, 5000, 7500), where uniform grids are employed. Results obtained are compared with the benchmark solutions provided by Ghia et al. [8] and Botella and Peyret [16]. The former was obtained using a multi-grid based finite-difference method with fine grids. For the latter, Chebyshev polynomials and analytic formulations were employed to handle the regular and singular parts of the solution and the benchmark results were given for $R_e = 100$ and $R_e = 1000$.

Using (20), for the two vertical walls, computational boundary conditions for the vorticity are obtained as follows

$$\omega_1 = \frac{\partial^2 \psi_1}{\partial x^2} = \sum_{i=1}^{N_x} \frac{d^2 \varphi_i(x_1)}{dx^2} \psi_i + \frac{d^2 \varphi_{N_x+1}(x_1)}{dx^2} \frac{\partial \psi_1}{\partial x} + \frac{d^2 \varphi_{N_x+2}(x_1)}{dx^2} \frac{\partial \psi_{N_x}}{\partial x}, \quad (31)$$

$$\omega_{N_x} = \frac{\partial^2 \psi_{N_x}}{\partial x^2} = \sum_{i=1}^{N_x} \frac{d^2 \varphi_i(x_{N_x})}{dx^2} \psi_i + \frac{d^2 \varphi_{N_x+1}(x_{N_x})}{dx^2} \frac{\partial \psi_1}{\partial x} + \frac{d^2 \varphi_{N_x+2}(x_{N_x})}{dx^2} \frac{\partial \psi_{N_x}}{\partial x}. \quad (32)$$

By means of point collocation and integration constants, derivative boundary values are thus incorporated into the 1D-IRBF approximations in an exact manner. They are forced to be satisfied exactly. Moreover, all grid points on the associated grid lines are used to compute ω_1 and ω_{N_x} . As a result, the present treatment possesses some global approximation properties. Expressions for ω at the two horizontal walls are obtained in an analogous manner. They are used for Scheme 1 and Scheme 2 and also for the present UW-CD and CD-CD techniques.

Original global and local 1D-IRBF versions are also implemented here. They are respectively similar to Scheme 1 and Scheme 2, except that the convection term is treated explicitly. The flow is considered to reach the steady state when the relative norm of the stream-function field between the two successive time levels, CM , is less than 10^{-8} . It can be seen from Figure 2 that the original 1D-IRBF versions diverge using time step of 0.01. In contrast, the present schemes produce converging solutions using the same time step. Scheme 1 and Scheme 2 require 11869 and 12485 iterations, respectively. Large time

steps can thus be used with the present schemes, making the convergence much faster as shown in Figure 3.

Results concerning the extreme values of the velocity profiles on the vertical and horizontal centreline for $Re = 1000$ are presented in Table 4. Both Scheme 1 and Scheme 2 produce results that are much closer to the spectral benchmark results than the UW-CD and CD-CD techniques. It can be seen that the UW-CD technique suffers from serious inaccuracy. Again, Scheme 1 is more accurate than Scheme 2.

At $Re = 5000$, the flow is simulated with the present schemes and the UW-CD technique. Contour plots for the stream function and the vorticity are shown in Figures 4 and 5, respectively. It can be seen that a secondary vortex in the region close to the top left corner by the UW-CD technique has a much smaller size than those produced by the present schemes. Figure 6 shows the velocity profiles on the vertical and horizontal centrelines, where results by Ghia et al. [8] are also included for comparison purposes. It can be seen that the UW-CD technique produces lower velocity extreme values than the present schemes. The present results are in very good agreement with those produced by Ghia et al. [8]. For the vorticity field, Scheme 1 produces a smoother solution than Scheme 2.

At $Re = 7500$, simulations are carried out with Scheme 1 and Scheme 2. A uniform grid of 131×131 is found to be sufficient for obtaining accurate results including the vorticity field as shown in Figure 7.

5.2.2 Triangular cavity

In contrast to the square cavity problem, the triangular-cavity flow presents a severe test for structured-grid-based numerical methods (e.g. [17]). Figure 8 shows the cavity geometry and boundary conditions. We take $P = \sqrt{3}$ and $Q = 3$. The velocity vectors imposed are $\mathbf{v} = (1, 0)^T$ for the lid and $\mathbf{v} = (0, 0)^T$ for the left and right walls. The

reference length and velocity are presently chosen as $L = Q/3$ and $U = 1$ (the velocity of the lid), respectively. It is noted that this problem was numerically studied by different techniques, including the finite-difference method (e.g. [18]) and the finite-element method (e.g. [19]). In early numerical studies, e.g. [18,20], finite differences were constructed on a transformed geometry and the flows were considered for $Re \leq 500$ only. Later on, solutions for higher Re numbers were achieved by means of, for example, the so-called computational boundary method in which the computational region under consideration is one-grid inside the physical domain [21] and the flow-condition-based interpolation [19].

At the lid, the imposition of boundary conditions for ω is similar to that used in the square cavity flow. At the left and right walls, analytic formulae for computing the vorticity boundary condition on a non-rectangular boundary [22] are utilised here:

$$\omega_b = \left[1 + \left(\frac{t_x}{t_y} \right) \right] \frac{\partial^2 \psi_b}{\partial x^2}, \quad (33)$$

for a x -grid line, and

$$\omega_b = \left[1 + \left(\frac{t_y}{t_x} \right) \right] \frac{\partial^2 \psi_b}{\partial y^2}, \quad (34)$$

for a y -grid line. In (33) and (34), t_x and t_y are the x - and y -components of the unit vector tangential to the boundary. The two formulae (33) and (34) require the approximations be conducted in one direction only. No exterior/fictitious points are used here.

Two Cartesian grids, namely Grid 1 (9702 points) and Grid 2 (15252 points), are employed to study the convergence of the solution. Unlike FDMs ([18,20]), the present schemes do not involve any coordinate transformations, making the processing simple. The flow is simulated at the Reynolds number of 0, 100, 200, 500, 1000, 1500 and 2000. If one takes a side of the triangular cavity as the length scale L , the actual Re will become $2\sqrt{3}$ times larger. For example, Re of 2000 is equivalent to a conventional Re of 6928. The advantage of Scheme 2 is its lower storage cost. Only Scheme 2 is employed here.

Its computer codes are run on a PC with the total physical memory of 1024 MB. To investigate the upwinding effects, an original local 1D-IRBF version is also employed. This version is similar to Scheme 2 except that the convection term is treated explicitly. As shown in Figure 9, a much larger time step can be used with Scheme 2 that converges much faster than the original local 1D-IRBF version.

Figures 10 and 11 present contour plots of the stream-function and vorticity fields, which look reasonable when compared with those available in the literature (e.g. [18,19]).

Figure 12 presents variations of the x component of the velocity vector on the vertical centreline $x = 0$ and the y component of velocity on the horizontal line $y = 2$. Results obtained in [19] are also included for comparison purposes. It can be seen that the velocity profiles using Grid 1 are almost identical to those using Grid 2. The present results agree well with those by the flow-conditioned-based interpolation FEM for all values of Re .

5.3 Discussion

Both the proposed method and the standard CV method employ the middle-point rule to evaluate line integrals associated with CV surfaces. However, for the proposed technique, the values at the CV faces are estimated using high-order 1D-IRBFs rather than the usual linear polynomials, and the convection term is treated using an upwind scheme with the deferred correction strategy. It can be seen that the construction of the 1D-IRBF approximations requires more computational effort than that of linear polynomials. However, the former can give superior accuracy. Given a grid size, the CPU time by the proposed method is greater than that by the standard CV method. However, for a prescribed accuracy, the standard CV method requires much more grid nodes than the proposed method. For instance, to obtain $N_e(\phi) = 4.2e - 5$ in Example 1, the numbers of nodes required are only 191 for Scheme 1 and up to about 10000 for the standard

CV method. It is noted that the value 10000 is obtained through extrapolation. For Scheme 1, the CPU time per iteration is approximately zero. For the standard CV method, at 4000 nodes (not 10000 nodes), the CPU time per iteration is already up to 0.359s. The computer codes are written using MATLAB and run on a Dell X86-based PC (Intel 2992 Mhz). In this regard (accuracy), the proposed method can be more efficient than the standard CV method. In addition, the employment of upwinding with 1D-IRBFs and deferred correction maintains the numerical stability or boundedness (first-order upwinding) and, at the same time, ensures high-order accuracy (1D-IRBFs).

6 Conclusions

This paper reports a new control-volume method, based on Cartesian grids and global/local 1D-IRBFs, for fluid-flow problems. A high-order upwind treatment with the deferred correction strategy using 1D-IRBFs for the convection term is implemented to enhance the stability property to the evolving solutions. The present schemes are able to produce converging solutions of high levels of accuracy at high values of the Reynolds number for both rectangular and non-rectangular fluid-flow domains.

Acknowledgement

This work is supported by the Australian Research Council. We would like to thank the referees for their helpful comments.

References

1. Patankar SV. *Numerical Heat Transfer and Fluid Flow*. McGraw-Hill: New York, 1980.

2. Huilgol RR, Phan-Thien N. *Fluid Mechanics of Viscoelasticity*. Elsevier: Amsterdam, 1997.
3. Gentry RA, Martin RE, Daly BJ. An Eulerian differencing method for unsteady compressible flow problems. *Journal of Computational Physics* 1966; **1**(1): 87-118.
4. Patankar SV. A calculation procedure for two-dimensional elliptic situations. *Numerical Heat Transfer, Part B* 1981; **4**(4): 409-425.
5. Leonard BP. A stable and accurate convective modelling procedure based on quadratic upstream interpolation. *Computer Methods in Applied Mechanics and Engineering* 1979; **19**(1): 59-98.
6. Leonard BP, Mokhtari S. Beyond first-order upwinding: The ultra-sharp alternative for non-oscillatory steady-state simulation of convection. *International Journal for Numerical Methods in Engineering* 1990; **30**(4): 729-766.
7. Khosla PK, Rubin SG. A diagonally dominant second-order accurate implicit scheme. *Computers & Fluids* 1974; **2**(2): 207-209.
8. Ghia U, Ghia KN, Shin CT. High-Re solutions for incompressible flow using the Navier-Stokes equations and a multigrid method. *Journal of Computational Physics* 1982; **48**: 387-411.
9. Fasshauer GE. *Meshfree Approximation Methods With Matlab* (Interdisciplinary Mathematical Sciences - Vol. 6). World Scientific Publisher: Singapore, 2007.
10. Kansa EJ. Multiquadrics- A scattered data approximation scheme with applications to computational fluid-dynamics-II. Solutions to parabolic, hyperbolic and elliptic partial differential equations. *Computers and Mathematics with Applications* 1990; **19**(8/9): 147-161.
11. Mai-Duy N, Tran-Cong T. Numerical solution of differential equations using multiquadric radial basis function networks. *Neural Networks* 2001; **14**(2): 185-199.

12. Mai-Duy N, Tanner RI. Solving high order partial differential equations with radial basis function networks. *International Journal for Numerical Methods in Engineering* 2005; **63**: 1636-1654.
13. Mai-Duy N, Tran-Cong T. Solving biharmonic problems with scattered-point discretisation using indirect radial-basis-function networks. *Engineering Analysis with Boundary Elements* 2006; **30**: 77-87.
14. Mai-Duy N, Tran-Cong T. A control volume technique based on integrated RBFNs for the convection-diffusion equation. *Numerical Methods for Partial Differential Equations* 2010; **26**(2): 426-447.
15. Boppana VBL, Gajjar JSB. Global flow instability in a lid-driven cavity. *International Journal for Numerical Methods in Fluids* 2010; **62**(8): 827-853.
16. Botella O, Peyret R. Benchmark spectral results on the lid-driven cavity flow. *Computers & Fluids* 1998; **27**(4): 421-433.
17. Jyotsna R, Vanka SP. Multigrid calculation of steady, viscous flow in a triangular cavity. *Journal of Computational Physics* 1995; **122**(1): 107-117.
18. Ribbens CJ, Watson LT, Wang C-Y. Steady viscous flow in a triangular cavity. *Journal of Computational Physics* 1994; **112**(1): 173-181.
19. Kohno H, Bathe K-J. A flow-condition-based interpolation finite element procedure for triangular grids. *International Journal for Numerical Methods in Fluids* 2006; **51**(6): 673-699.
20. McQuain WD, Ribbens CJ, Wang C-Y, Watson LT. Steady viscous flow in a trapezoidal cavity. *Computers & Fluids* 1994; **23**(4): 613-626.
21. Li M, Tang T. Steady viscous flow in a triangular cavity by efficient numerical techniques. *Computers & Mathematics with Applications* 1996; **31**(10): 55-65.

22. Le-Cao K, Mai-Duy N, Tran-Cong T. An effective integrated-RBFN Cartesian-grid discretisation for the stream function-vorticity-temperature formulation in non-rectangular domains. *Numerical Heat Transfer, Part B* 2009; **55**(6): 480-502.

Table 1: Burgers equation, $x_A = -0.1, x_B = 0.1, \varepsilon = 10^{-3}, tol = 10^{-7}, \phi(x, 0) = (\phi_B - \phi_A)/(x_B - x_A)x$, time-marching solver: convergence study for the original IRBF version and the two present schemes. Converging and diverging solutions are denoted as \checkmark and x, respectively.

Original IRBF version						
Δt	N					
	51	61	71	81	91	101
0.1	x	x	x	x	x	x
0.05	x	x	x	x	x	x
0.01	x	x	x	x	x	x
0.005	x	x	x	x	x	x
0.001	\checkmark	\checkmark	\checkmark	\checkmark	\checkmark	\checkmark
Scheme 2						
Δt	N					
	51	61	71	81	91	101
0.1	x	x	\checkmark	\checkmark	\checkmark	\checkmark
0.05	x	\checkmark	\checkmark	\checkmark	\checkmark	\checkmark
0.01	x	\checkmark	\checkmark	\checkmark	\checkmark	\checkmark
0.005	x	\checkmark	\checkmark	\checkmark	\checkmark	\checkmark
0.001	\checkmark	\checkmark	\checkmark	\checkmark	\checkmark	\checkmark
Scheme 1						
Δt	N					
	51	61	71	81	91	101
0.1	x	\checkmark	\checkmark	\checkmark	\checkmark	\checkmark
0.05	\checkmark	\checkmark	\checkmark	\checkmark	\checkmark	\checkmark
0.01	\checkmark	\checkmark	\checkmark	\checkmark	\checkmark	\checkmark
0.005	\checkmark	\checkmark	\checkmark	\checkmark	\checkmark	\checkmark
0.001	\checkmark	\checkmark	\checkmark	\checkmark	\checkmark	\checkmark

Table 2: Burgers equation, $x_A = -0.1, x_B = 0.1, \varepsilon = 10^{-3}, tol = 10^{-7}, \phi(x, 0) = (\phi_B - \phi_A)/(x_B - x_A)x, \Delta t = 0.001$: accuracy by the UW-CD method and by the present schemes. It is noted that the error $N_e(\phi)$ is computed at a test set of 501 uniformly distributed points.

N	h	$N_e(\phi)$		
		UW-CD	Scheme 2	Scheme 1
51	4.00e-3	3.74e-2	3.59e-2	2.23e-2
61	3.33e-3	2.81e-2	2.38e-2	1.40e-2
71	2.85e-3	2.21e-2	1.66e-2	8.88e-3
81	2.50e-3	1.81e-2	1.19e-2	5.63e-3
91	2.22e-3	1.54e-2	8.75e-3	3.58e-3
101	2.00e-3	1.33e-2	6.75e-3	2.28e-3
111	1.81e-3	1.19e-2	5.13e-3	1.45e-3
121	1.66e-3	1.08e-2	4.14e-3	9.25e-4
131	1.53e-3	9.93e-3	3.45e-3	5.90e-4
141	1.42e-3	9.22e-3	2.86e-3	3.77e-4
151	1.33e-3	8.61e-3	2.49e-3	2.41e-4
161	1.25e-3	8.03e-3	2.27e-3	1.55e-4
171	1.17e-3	7.49e-3	2.10e-3	1.00e-4
181	1.11e-3	7.20e-3	1.90e-3	6.52e-5
191	1.05e-3	6.82e-3	1.76e-3	4.26e-5

Table 3: Burgers equation, $x_A = -0.1, x_B = 0.1, \varepsilon = 10^{-3}, tol = 10^{-7}, \phi(x, 0) = (\phi_B - \phi_A)/(x_B - x_A)x, \Delta t = 0.005$: convergence rates by Scheme 1.

h	Convergence rates
4.00e-3	-
3.33e-3	$O(h^{2.54})$
2.85e-3	$O(h^{2.97})$
2.50e-3	$O(h^{3.40})$
2.22e-3	$O(h^{3.84})$
2.00e-3	$O(h^{4.29})$
1.81e-3	$O(h^{4.73})$
1.66e-3	$O(h^{5.17})$
1.53e-3	$O(h^{5.61})$
1.42e-3	$O(h^{6.03})$
1.33e-3	$O(h^{6.45})$
1.25e-3	$O(h^{6.84})$
1.17e-3	$O(h^{7.21})$
1.11e-3	$O(h^{7.55})$
1.05e-3	$O(h^{7.85})$

Table 4: Square-cavity flow, $Re = 1000$: Percentage errors relative to the spectral benchmark results for the extreme values of the velocity profiles on the centrelines.

Grid	Errors (%) for u_{min}			
	UW-CD	CD-CD	Scheme 2	Scheme 1
31×31	46.10	29.19	12.85	11.86
41×41	38.17	18.13	7.92	6.50
51×51	32.92	12.11	5.34	4.09
61×61	29.12	8.63	3.80	2.80
71×71	26.21	6.46	2.81	2.03
81×81	23.88	5.02	2.14	1.54
91×91	21.95	4.01	1.66	1.19
101×101	20.33	3.28	1.32	0.96
111×111	18.94	2.73	1.05	0.78
121×121	17.74	2.31	0.84	0.65
131×131	16.69	1.98	0.65	0.55

Grid	Errors (%) for v_{max}			
	UW-CD	CD-CD	Scheme 2	Scheme 1
31×31	48.01	29.98	13.05	11.91
41×41	39.71	18.45	8.02	6.55
51×51	34.43	12.32	5.40	4.13
61×61	30.62	8.79	3.84	2.83
71×71	27.68	6.58	2.83	2.05
81×81	25.31	5.12	2.14	1.56
91×91	23.34	4.09	1.66	1.21
101×101	21.67	3.35	1.31	0.97
111×111	20.23	2.79	1.04	0.79
121×121	18.98	2.36	0.82	0.66
131×131	17.89	2.02	0.62	0.56

Grid	Errors (%) for v_{min}			
	UW-CD	CD-CD	Scheme 2	Scheme 1
31×31	40.12	29.83	12.65	11.53
41×41	30.42	18.08	7.72	6.25
51×51	24.70	11.90	5.13	3.87
61×61	20.94	8.40	3.58	2.58
71×71	18.24	6.25	2.64	1.85
81×81	16.19	4.83	2.00	1.39
91×91	14.56	3.85	1.55	1.07
101×101	13.24	3.14	1.23	0.85
111×111	12.14	2.61	0.99	0.70
121×121	11.22	2.20	0.79	0.58
131×131	10.42	1.88	0.63	0.49

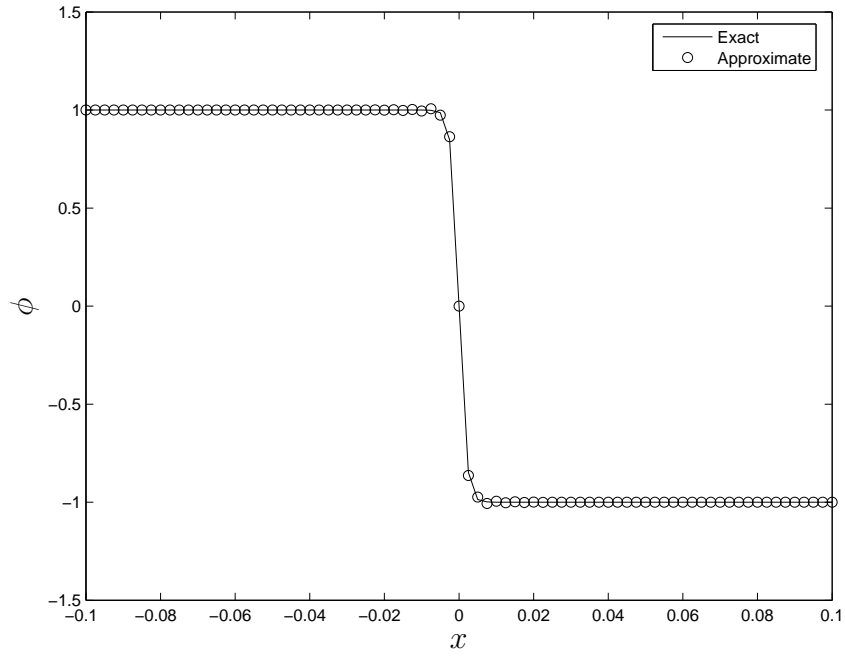


Figure 1: Burgers equation, $x_A = -0.1, x_B = 0.1, \varepsilon = 10^{-3}, tol = 10^{-7}, \phi(x, 0) = (\phi_B - \phi_A)/(x_B - x_A)x, N = 81$: approximate solution by Scheme 1.

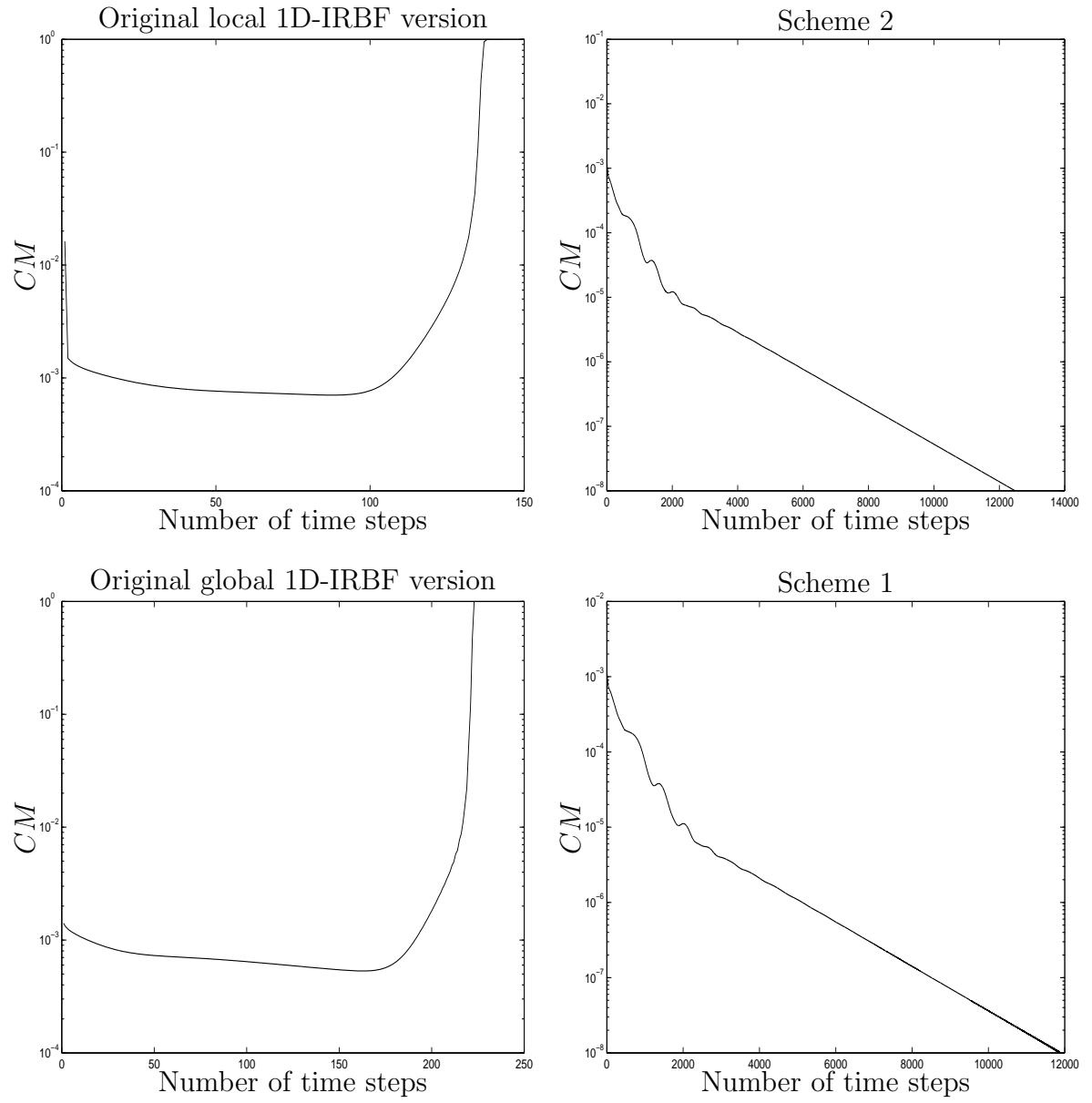


Figure 2: Square-cavity flow, $Re = 1000$, 81×81 , solution at $Re = 400$ used as initial guess, time step of 0.01: convergence behaviour. It is noted that CM denotes the relative norm of the stream-function field between two successive time levels.

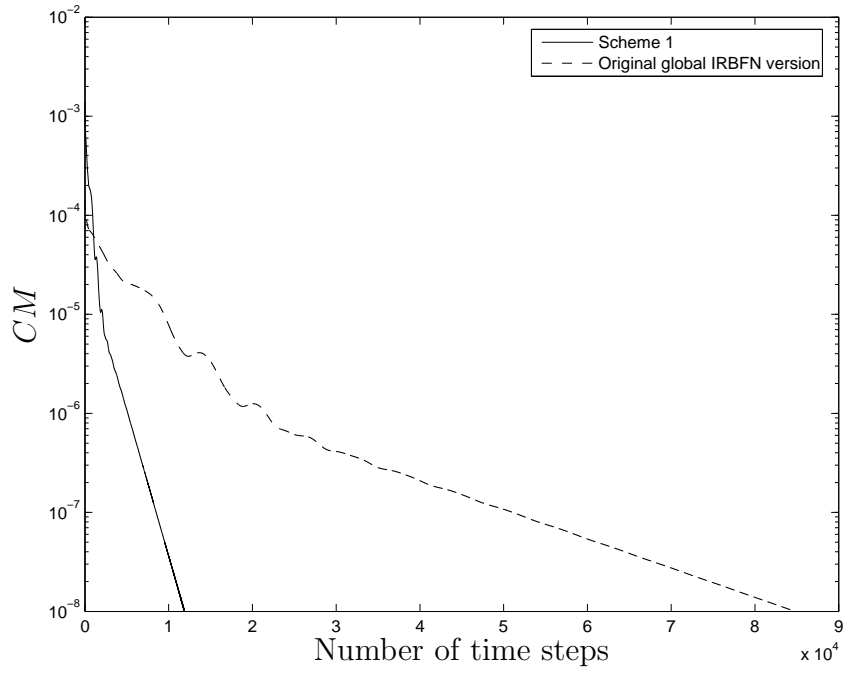
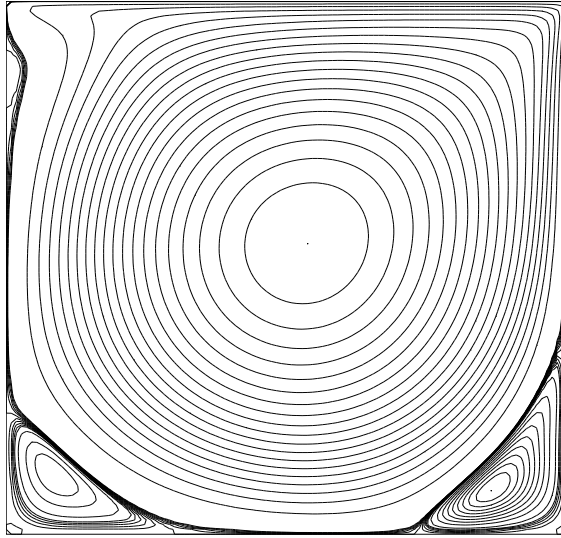
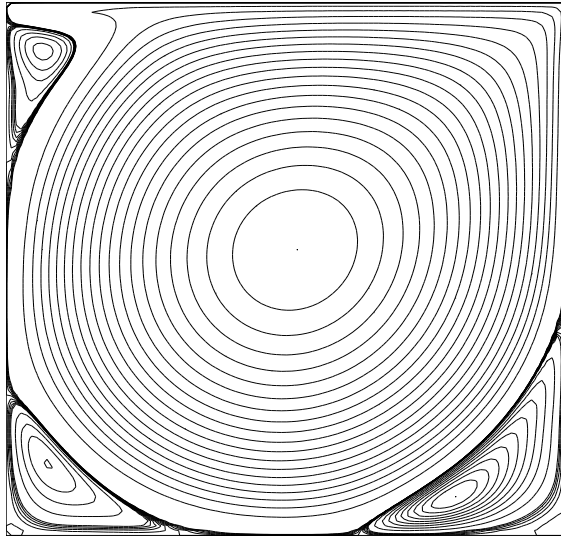


Figure 3: Square-cavity flow, $Re = 1000$, 81×81 , solution at $Re = 400$ used as initial guess: convergence behaviour. Scheme 1 using time step of 0.01 converges much faster than the original global 1D-IRBFN version using time step of 0.001. It is noted that the latter diverges for time step of 0.01. CM denotes the relative norm of the stream-function field between two successive time levels.

UW-CD



Scheme 2



Scheme 1

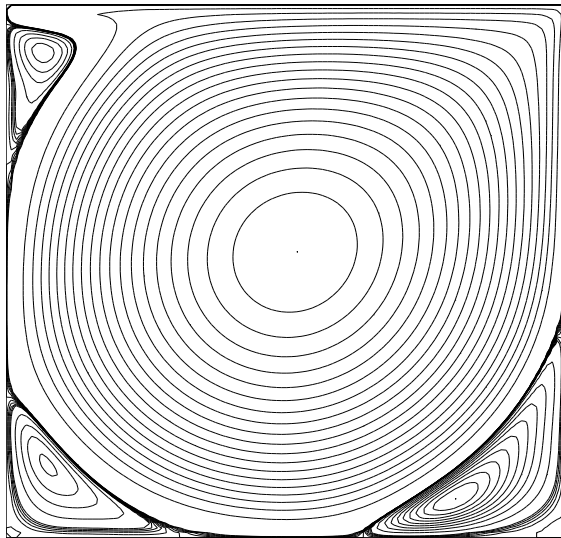
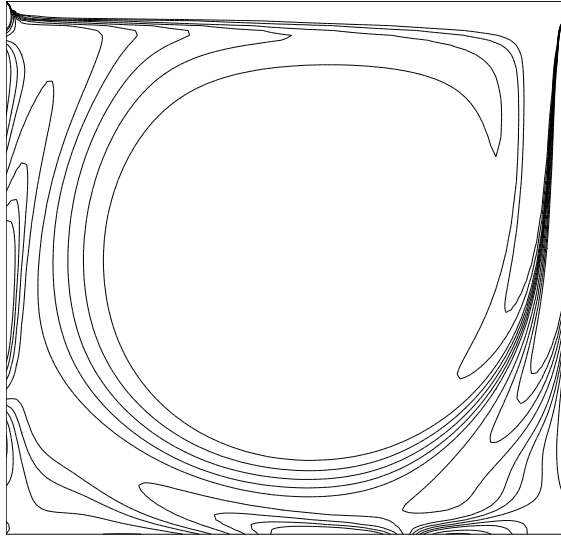
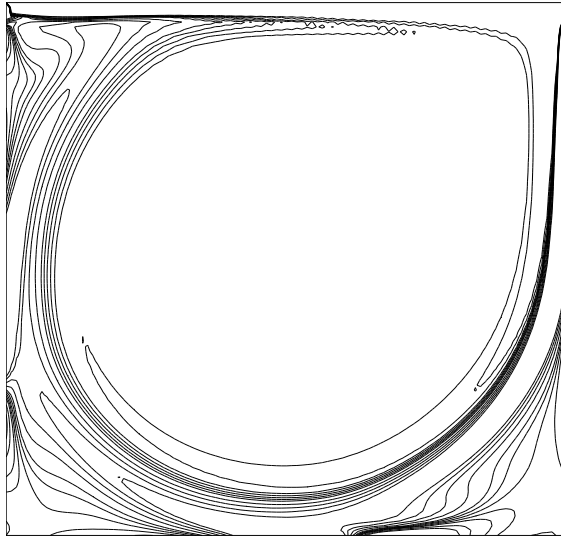


Figure 4: Square-cavity flow: contour plots for the stream function at $R_e = 5000$ using a grid of 111×111 .

UW-CD



Scheme 2



Scheme 1

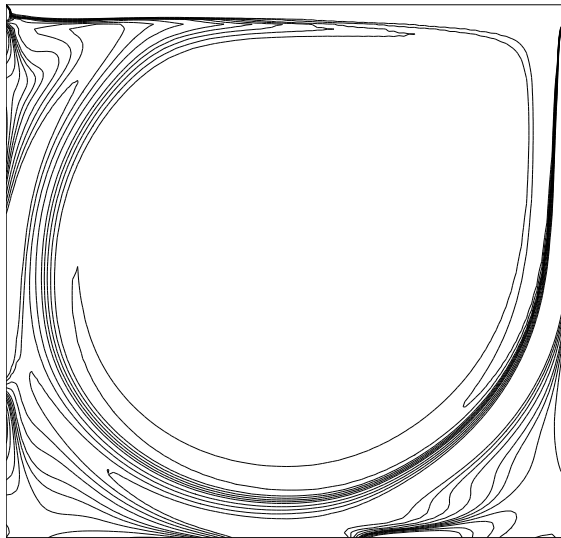


Figure 5: Square-cavity flow: contour plots for the vorticity at $R_e = 5000$ using a grid of 111×111 .

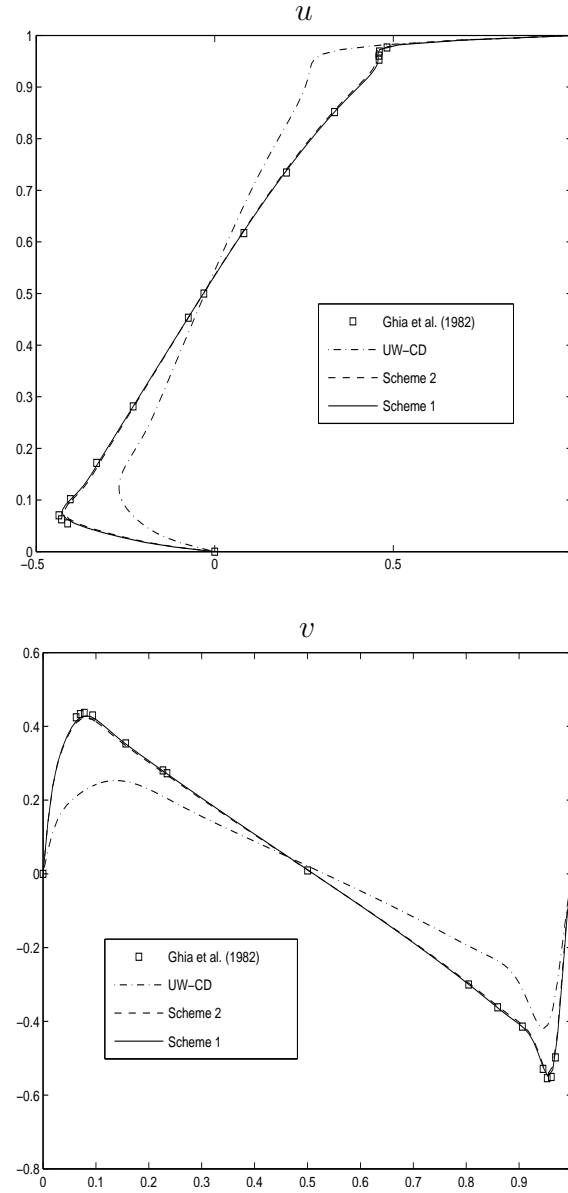


Figure 6: Square-cavity flow: velocity profiles by the UW-CD technique, Scheme 2 and Scheme 1 at $R_e = 5000$ using a grid of 111×111 . Results by Ghia et al. [8] are also included for comparison purposes.

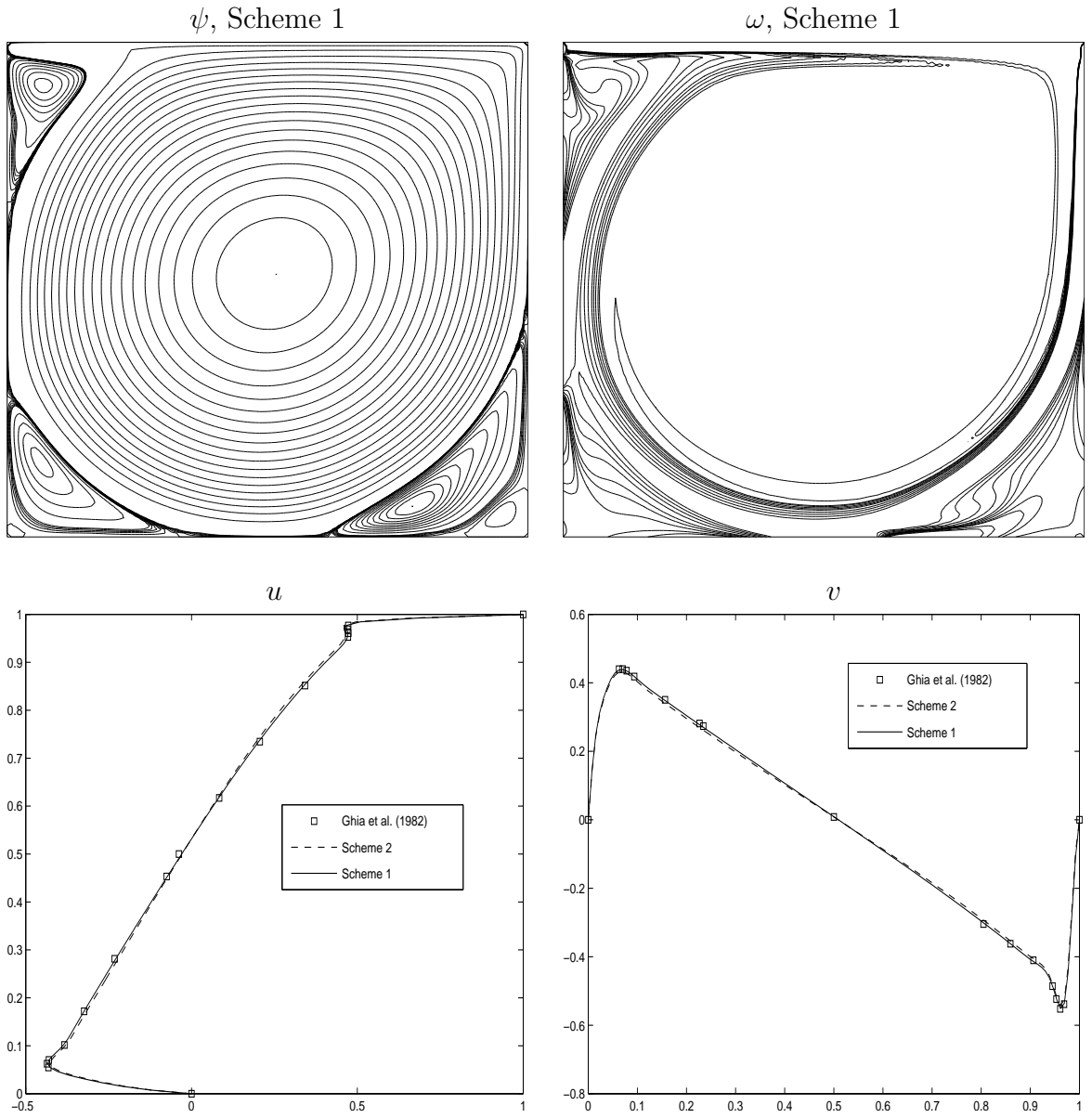


Figure 7: Square-cavity flow: Solutions at $Re = 7500$ using a uniform grid of 131×131 by Scheme 1 and Scheme 2. Velocity profiles by Ghia et al. [8] are also included for comparison purposes.

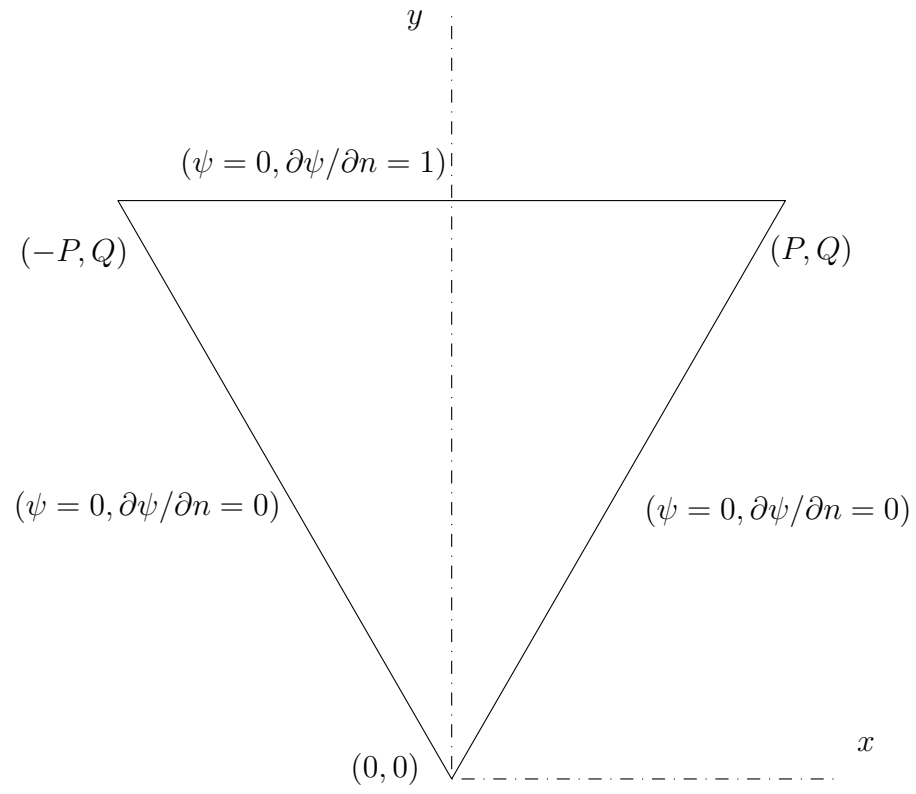


Figure 8: Triangular-cavity flow: geometry and boundary conditions.

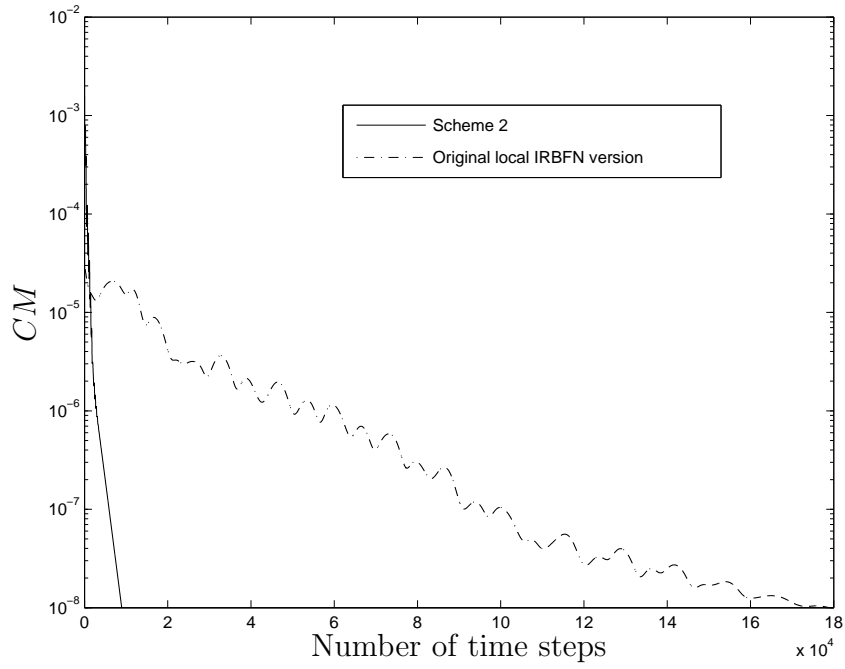


Figure 9: Triangular-cavity flow, $Re = 1000$, grid of 9702 points, solution at $Re = 500$ used as initial guess: convergence behaviour. Scheme 2 using time step of 0.01 converges much faster than the original local 1D-IRBF version using time step of 0.001. It is noted that the latter diverges for time step of 0.01. CM denotes the relative norm of the stream-function field between two successive time levels.

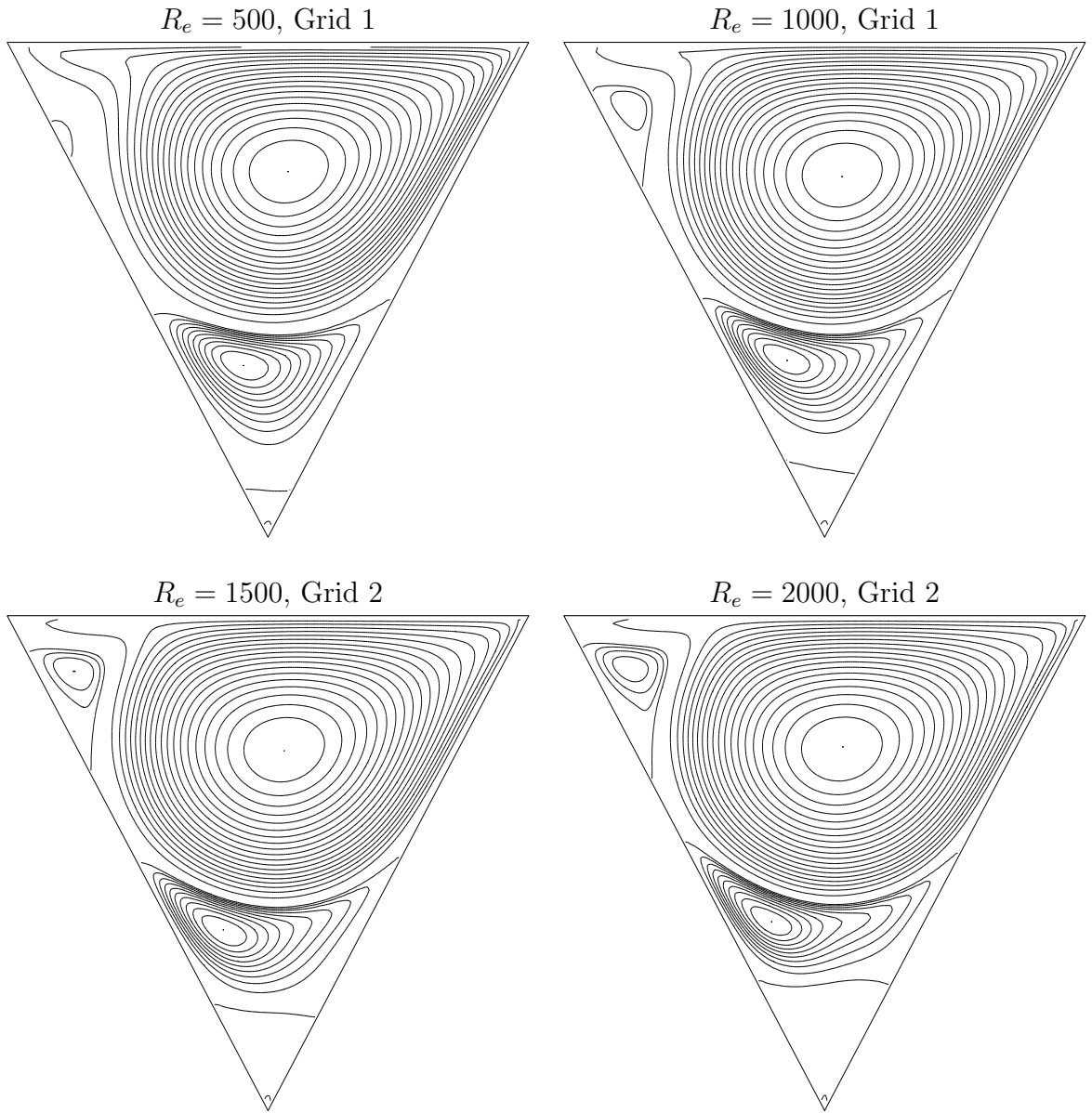


Figure 10: Triangular-cavity flow: Contour plots of the stream-function field using Scheme 2.

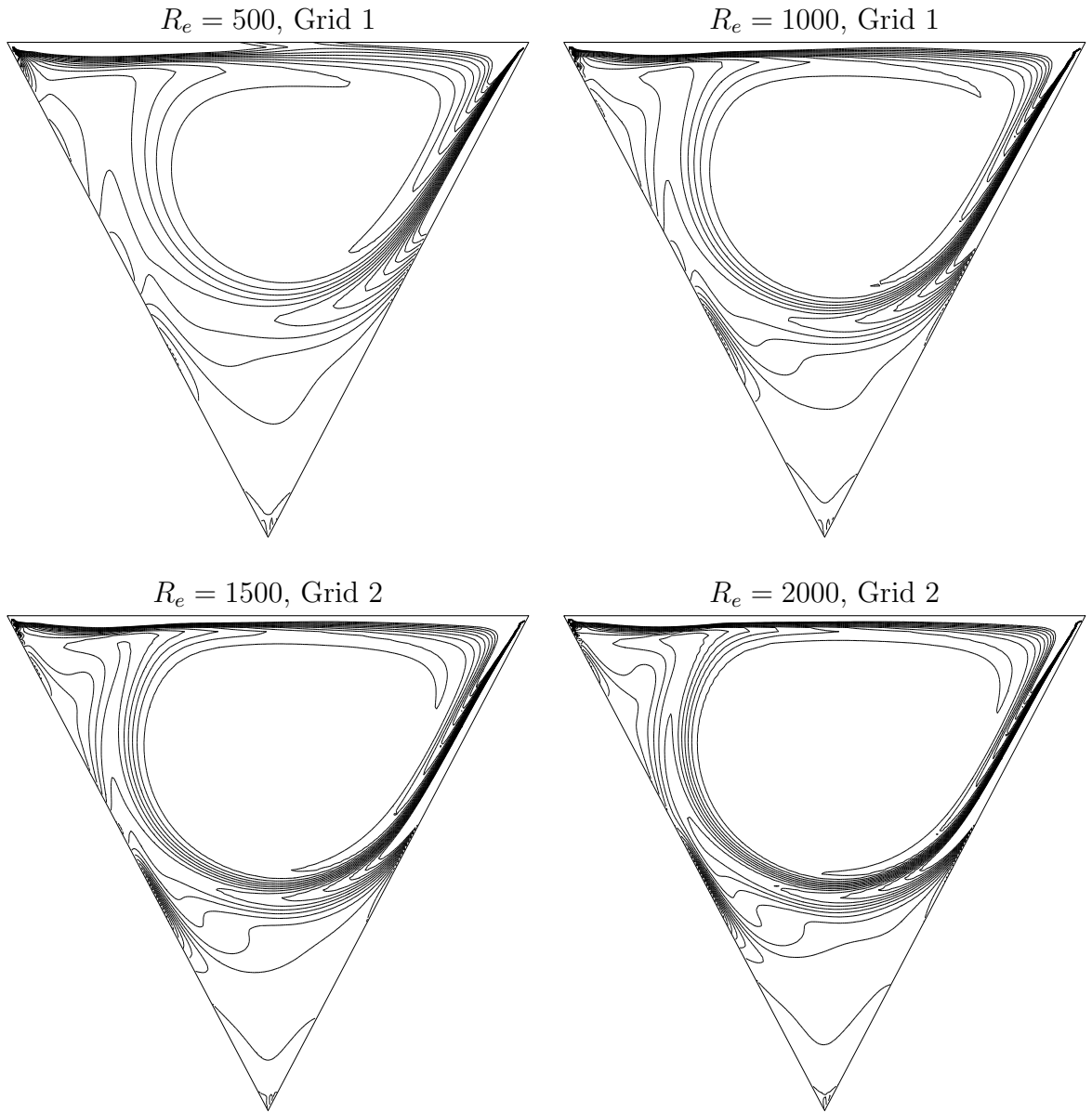


Figure 11: Triangular-cavity flow: Contour plots of the vorticity field using Scheme 2.

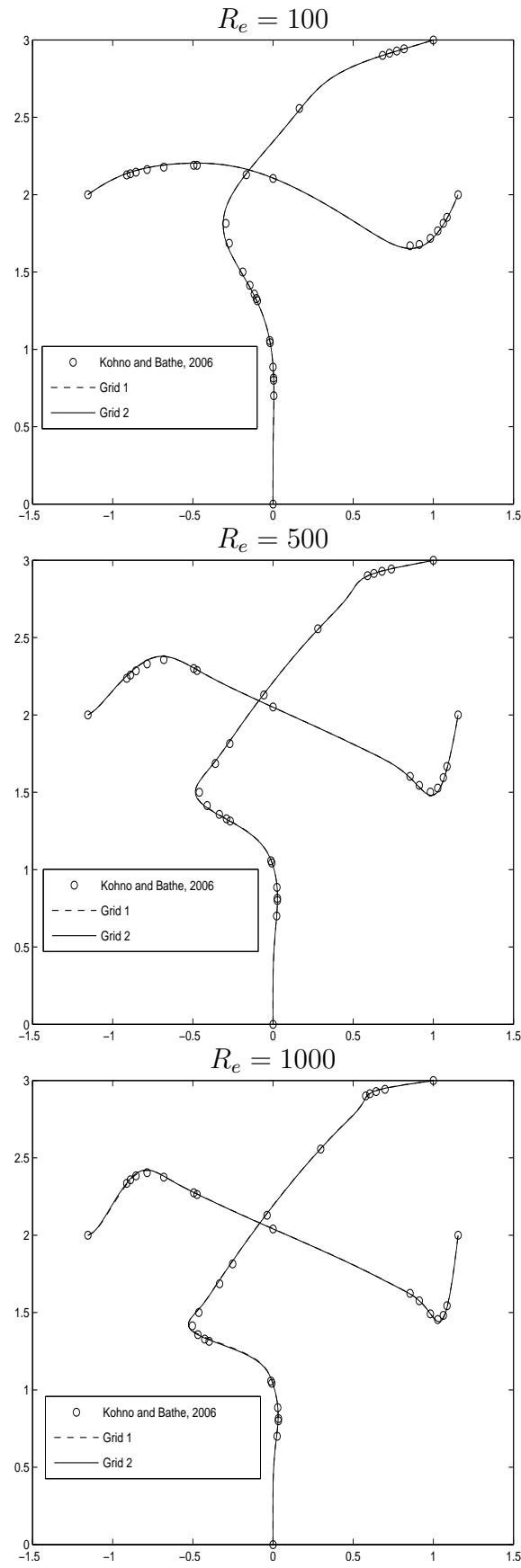


Figure 12: Triangular-cavity flow: Velocity profiles by Scheme 2 and the flow-condition-based interpolation FEM [19].